RSC Advances

ROYAL SOCIETY OF CHEMISTRY

PAPER

View Article Online
View Journal | View Issue

Check for updates

Cite this: *RSC Adv.*, 2025, **15**, 29404

Improving the thermoelectric properties of $Ca_3Co_4O_9$ by reducing thermal conductivity through composite nano-ZnO

Yanan Li,[a] Ping Wu,*[b] Shuai Ma,*[c] Mingdi Zhang[d] and Yili Pei[b]

Received 8th July 2025
Accepted 14th August 2025

DOI: 10.1039/d5ra04876a

rsc.li/rsc-advances

Composite nanomaterial is a scientific solution to modulating the properties of thermoelectric materials. The thermoelectric properties of $Ca_3Co_4O_9$ ceramic that remain stable in high-temperature air are relatively low, and how to decouple the relationship between heat and electricity is the focus of the research. This study systematically investigates the thermoelectric transport properties of composite $Ca_3Co_4O_9$@xZnO materials. The samples do not undergo additional chemical reactions and exhibit lamellar microstructures. At temperatures up to 825 K, the thermal conductivity of pure $Ca_3Co_4O_9$ was determined to be 2.58 W m^{-1} K^{-1}, whereas that of the $Ca_3Co_4O_9$@0.7ZnO was significantly reduced to 1.94 W m^{-1} K^{-1}, a reduction of about 25%. Based on the effective medium theory analysis, adding ZnO in $Ca_3Co_4O_9$ introduces interfacial thermal resistance and porosity, which is key in reducing thermal conductivity. Adding ZnO promotes the electrical conductivity enhancement of $Ca_3Co_4O_9$ with a minor reduction in the Seebeck coefficient. Under the coordinated regulation of electrical and thermal properties, the *ZT* of $Ca_3Co_4O_9$@0.7ZnO is enhanced by about 75% compared with that of pure $Ca_3Co_4O_9$.

Introduction

Thermoelectric materials, as a jewel in the field of new energy materials, with their unique properties – direct and efficient conversion between heat and electricity through the movement of carriers inside the materials – have shown remarkable potential for application.[1] As scientific research continues, the family of thermoelectric materials is gradually expanding its range of systems, from oxide, SiGe, and SnSe in the high-temperature region to Pb–Te and Mg–Si alloys in the medium-temperature range to Bi_2Te_3 in the room-temperature region.[2–6] Oxide thermoelectric materials are also favored for their excellent thermostability, relatively low cost, and environmental protection, especially among the oxide thermoelectric material systems such as Na–Co–O, Bi–Sr–Co–O, Ca–Mn–O and Ca–Co–O.[7–11] $Ca_3Co_4O_9$ has garnered significant research attention owing to its exceptional thermoelectric properties and stability at elevated temperatures. It demonstrates significant practical utility and expansive potential in thermoelectric conversion technology.

The core assessment index for the conversion effectiveness of thermoelectric materials is the dimensionless quality factor, defined as $ZT = \sigma S^2 T/(\kappa_c + \kappa_l)$, where σ stands for electrical conductivity; S is the Seebeck coefficient; κ_c denotes the thermal conductivity of carriers; κ_l stands for thermal conductivity of the lattice. To achieve high thermoelectric conversion efficiency, the following conditions must be met: high σ to guarantee efficient charge transport, high Seebeck coefficient to produce a significant thermoelectric effect, and low $(\kappa_c + \kappa_l)$ to reduce heat loss. However, the *ZT* values of polycrystalline $Ca_3Co_4O_9$ remain low due to the strong interdependence between the abovementioned parameters. Among the four thermoelectric parameters, the κ_l is the only one that can be independently tuned, improving the thermoelectric properties. The κ_l can be diminished through enhanced phonon scattering, and the main strategies include the introduction of point defects, dislocations, and interfacial scattering. In addition to introducing atomic size point defects by common ion doping,[12–14] interfacial scattering is another important means of modulation. Interfacial scattering mainly affects low-frequency phonons and involves submicron scattering at grain boundaries and the interface between the second phase and the substrate. Heterogeneous interfaces can be increased by grain refinement, preparation of nano-precipitated phases, or direct composite nano-second phases. The additional barrier generated at the interface produces additional scattering of the carriers, suppressing their transport and reducing the mobility while enhancing the energy dependence of the carrier relaxation time and boosting the scattering factor value, increasing the Seebeck coefficient.[15] In addition, introducing the nano-second phase forms a potential barrier, scatters low-energy

---

[a] College of Science, North China University of Technology, Beijing 100144, China
[b] School of Mathematics and Physics, University of Science and Technology Beijing, Beijing 100083, China. E-mail: pingwu@sas.ustb.edu.cn
[c] School of Mechanical Engineering, Tianjin University of Commerce, Tianjin 300134, China. E-mail: mashal0611@163.com
[d] Rocket Force University of Engineering, Xi'an 710025, China

carriers, produces an energy filtering effect, and raises the average carrier energy, further increasing the Seebeck coefficient.[16] The composite of nanomaterials as the second phase into $Ca_3Co_4O_9$ reduces the grain size and generates grain boundaries between the composite and the matrix. The rise in grain boundary density boosts long-wavelength phonon scattering, reducing lattice thermal conductivity. Therefore, the composite nanosecond phase is of significant research significance and value for optimizing the properties of thermoelectric materials.

Previous studies have revealed the diverse effects of SiO_2, ZrO_2, SiC, and Co_3O_4 composites with $Ca_3Co_4O_9$ on their thermoelectric properties.[17–20] In the previous work of our research team, by compositing nano second-phase materials $MoSi_2$ and carbon nanotubes with $Ca_3Co_4O_9$,[21] we have adjusted for the electrical conductivity of $Ca_3Co_4O_9$. Still, we have also significantly reduced its thermal conductivity. Based on an in-depth analysis of the effective medium theory and the series-parallel model, combined with actual measured thermal conductivity data, we find that the composite nanoscale second-phase material introduces additional scattering centers, interfacial thermal resistance, and pore structure, which together effectively reduce the thermal conductivity. Specifically, the σ of the $Ca_3Co_4O_9/0.1MoSi_2$ composite sample is enhanced to 83.16 S cm^{-1}, a 49.2% increase in electrical conductivity compared to that of the pure $Ca_3Co_4O_9$. Thermal conductivity of $Ca_3Co_4O_9/0.4MoSi_2$ decreased to 1.26 W m^{-1} K^{-1} at 1080 K, showing enhanced performance over pure $Ca_3Co_4O_9$ (1.74 W m^{-1} K^{-1}), a substantial thermal conductivity reduction was achieved.[21] In addition, the *ZT* of the composite reaches 0.26, which is nearly 44.4% higher compared to the pure sample, and this result fully demonstrates the remarkable effect of the composite nanoscale second-phase material in optimizing the thermoelectric properties of $Ca_3Co_4O_9$.

The incorporation of composite nanosecond phases leads to the formation of defects within the material. While these defects are beneficial for lowering thermal conductivity, they simultaneously hinder carrier mobility, adversely impacting electrical conductivity. The primary source of this phenomenon is that the nanoscale second phase can hinder the carrier transport path. Therefore, it is imperative to rationally regulate the distribution and morphology of the nanoscale second phase and its interfacial state with the substrate material. Compared with SiO_2, ZrO_2, SiC, Co_3O_4 and other oxides mentioned in the introduction, adding ZnO[22] with an energy bandgap of 3.37 eV—a critical feature enabling potential electrical conductivity enhancement while suppressing thermal transport. In addition, ZnO is not only inexpensive and easy to prepare but also has excellent conductivity and good thermal stability, which has shown potential for broad application in a variety of fields, such as supercapacitors, solar cells, sensors, and high-temperature thermoelectric materials. Although Luo's group[23] has investigated the Seebeck coefficient ($\sim$119.3 μV K^{-1}) and electrical properties of $Ca_3Co_4O_9$/ZnO heterostructures by using pulsed laser deposition technique, the study on the composites of ZnO and $Ca_3Co_4O_9$ ceramic materials and their effects on the thermoelectric properties have not been reported.

This research involved the synthesis of $Ca_3Co_4O_9@x$ZnO through the sol–gel method, employing atmospheric pressure sintering. A comprehensive analysis was conducted to explore how incorporating ZnO influences the thermoelectric performance of $Ca_3Co_4O_9$. The results show that adding ZnO in suitable amounts reduces thermal conductivity and enhances electrical conductivity in $Ca_3Co_4O_9$ ceramics, optimizing their thermoelectric properties.

Experimental

$Ca_3Co_4O_9$ and its composite ceramic powder samples with ZnO were prepared using the sol–gel method. $Ca(NO_3)_2\cdot 4H_2O$ (7.085 g), $Co(NO_3)_2\cdot 6H_2O$ (11.641 g), citric acid monohydrate (16.181 g), and different amounts of ZnO (0 g, 0.1 g, 0.3 g, 0.5 g, 0.7 g) were dissolved in deionized water (100 ml) in specific proportions and mixed well. Subsequently, it was heated and stirred at 363 K until gel formation occurred. The wet gel was dried at 393 K for 12 hours and then milled to get the powder. Next, the precursor powder was subjected to self-propagating combustion at 573 K. After grinding again, it was calcined in the air atmosphere at 1073 K for 12 h. Subsequently, the powders were pressed under 30 MPa, keep under pressure for 20 minutes, and finally sintered at 1073 K for 16 hours. Depending on the ZnO content, the resulting samples were abbreviated as CCO@*x*ZnO (x = 0, 0.1, 0.3, 0.5, 0.7). X-ray diffraction (XRD, Rigaku D/max2500, Cu target, Kα-ray) analyzed the samples' phase composition. The working voltage of the X-ray tube is 40 kV, the working current is 200 mA, and the scanning speed and scanning angle step size are 5° min^{-1} and 0.01°, respectively. The scanning electron microscope (Zeiss Supra 55) was utilized for morphological examination. X-ray photoelectron spectroscopy (XPS) was conducted using the PHI5000VersaProbe III system from ULVAC-PHI to delve deeper into the surface chemistry of the samples. This setup featured a monochromatic Al Kα X-ray source, operating at 1486 eV, to provide precise insights into the chemical states present. Elemental compositions of the samples were quantified through Avantage XPS software, which yielded component peaks. Netzsch SBA458 (four-probe method) measured electrical conductivity and the Seebeck coefficient. The instrument used in Hall test is Ecopia Hall effect tester (HMS-7000). Thermal conductivity was calculated by laser scattering (Netzsch Instruments/LAF467) in combination with the thermal diffusion coefficient D, specific heat capacity C_p, and the geometric density of the sample d.

Results and discussion

Phase composition and microstructure

Fig. 1a illustrates the XRD patterns of each sample of CCO@*x*ZnO which shows that no generation of the second phase was detected except for ZnO. The inset of Fig. 1 provides a locally magnified view of the (100) diffraction peak of ZnO. Owing to the relatively low content of ZnO, the peak intensity is weak; however, it is evident that the intensity of this peak increases correspondingly with the increase in ZnO content. The SEM images Fig. 1b–f reveal that the samples exhibit

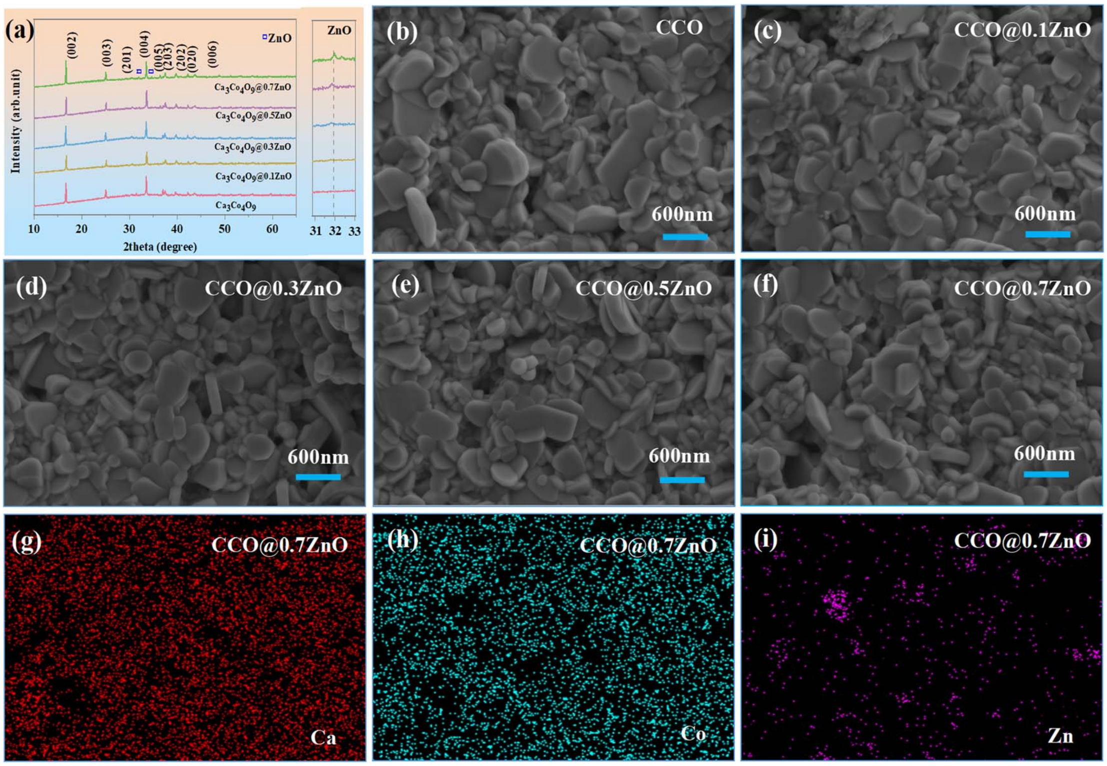

Fig. 1 (a) XRD pattern, (b–f) SEM pattern, and (g–i) CCO@0.7ZnO main element distribution map of CCO@*x*ZnO.

lamellar structural features, which coincide with the apparent preferential orientation in the (00*l*) direction in the XRD patterns, indicating a tendency for preferential grain growth in this direction. Notably, the morphology of the samples did not change significantly with the increasing amount of nano ZnO addition. The presence of ZnO particles can be identified by further observation of the elemental surface distribution map of the CCO@0.7ZnO samples. Based on the energy dispersive spectroscopy data (Table 1), we calculated the atomic ratio of Ca and Co, and the results showed that the ratio of Ca : CO increased slightly with the increase of ZnO content. In addition, the density of the samples shows a tendency to increase with increasing ZnO content. Mainly attributed to two reasons, on the one hand, the theoretical density of ZnO (5.6 g cm^{-3}) is higher than that of $Ca_3Co_4O_9$ (about 3.6 g cm^{-3}). The micro nano ZnO particles can migrate to the pores or grain boundaries between the matrix particles, play the role of physical filling, reduce the pores, so that the average density of the composite will increase with the increase of ZnO content. On the other hand, ZnO nanoparticles have high specific surface area and surface activity. During the sintering process, this high surface energy is the driving force of material diffusion. As the activation center, it helps to accelerate the grain boundary movement, pore shrinkage and material rearrangement, making the composite sample more compact.

Table 1 Atomic content, atomic ratios, and apparent densities of CCO@*x*ZnO

	Atomic content				Atomic ratios		
Sample	Ca	Co	Zn	O	Ca : Co	Zn : O	Densities (g cm^{-3})
CCO	22.62	30.06	0	47.32	0.75	0	3.559
CCO@0.1ZnO	22.26	28.67	0.37	48.70	0.78	0.01	3.729
CCO@0.3ZnO	24.33	27.32	0.45	49.90	0.82	0.02	3.787
CCO@0.5ZnO	23.63	28.32	1.03	47.72	0.83	0.04	3.820
CCO@0.7ZnO	24.44	28.53	1.53	45.50	0.86	0.05	3.827

To explore the ionic state of the elements in the samples and the specific effect of the composite ZnO on the ionic ratios, the samples were tested in detail using XPS analysis. Fig. 2a illustrates the XPS full-spectrum scan results for each sample of CCO@*x*ZnO, and the locations of the individual characteristic peaks have been clearly labeled. As shown in Fig. 2b, the XPS spectrum shows the characteristic peak of Zn 2p in ZnO (Zn $2p_{3/2}$ at 1021.8 eV and Zn $2p_{1/2}$ at 1044.9 eV). The peak of Zn 2p is relatively weak, but the intensity of the peak increases slightly with the increase of ZnO content.

Given that calcium and cobalt are the primary metal ion components in the sample, with cobalt being present in relatively high concentrations, high-resolution XPS spectra of the Co 2p region were selected for detailed analysis (Fig. 3a–e) to obtain precise data. The Co 2p spectrum reveals two distinct spin–orbit splitting peaks: for the undoped sample, the Co $2p_{3/2}$ and Co $2p_{1/2}$ maxima occur at 779.93 eV and 795.33 eV, respectively. For Co^{3+}, the $2p_{3/2}$ and $2p_{1/2}$ peaks are observed at

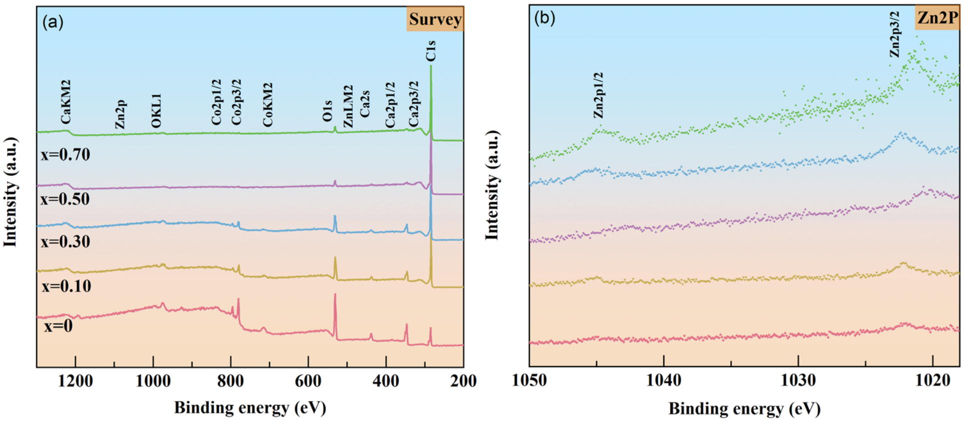

Fig. 2 (a) XPS full spectra of CCO@*x*ZnO and (b) Zn 2p high-resolution spectrum.

779.6 eV and 794.8 eV, respectively, while for Co^{4+}, these peaks shift to 781.4 eV and 796.8 eV. These binding energies fall within the expected ranges for Co^{3+} and Co^{4+}. Additionally, a satellite peak occurs near 790.5 eV, attributed to Co^{3+}. To assess the influence of composite ZnO on the properties of the sample, a peak fitting analysis was performed on the high-resolution Co 2p spectra (Fig. 3a–e). The Co^{3+}/Co^{4+} ratio was determined from the area ratios of their peaks in Fig. 3f. As the ZnO content increased, the Co^{3+}/Co^{4+} ratio remained stable at approximately 0.9, showing minimal variation. Furthermore, EDS data (Table 1) indicate that the Ca/Co atomic ratio remained nearly constant with increasing ZnO. Since previous XPS analysis confirmed the stability of Co content, it is inferred that the Ca content also remains unchanged, suggesting that ZnO does not participate in substitutional reactions within the sample but instead functions as a nanoscale additive at the pores of $Ca_3Co_4O_9$. This is consistent with XRD analysis results.

Thermal transport properties

Experimental values of thermal conductivity. Fig. 4a and b show the thermal diffusivity and specific heat capacity of CCO@*x*ZnO. The graph shows that the specific heat capacity remains almost unchanged while the thermal diffusion coefficient of the sample with added ZnO decreases. The thermal conductivity can be obtained based on the thermal diffusion coefficient, specific heat capacity, and density. Fig. 4d presents the total thermal conductivity (κ) as a function of temperature for the CCO@*x*ZnO series of samples. By resolving the embedded plot in Fig. 4c, all samples exhibit low thermal conductivity due to the inherent lamellar construction property of $Ca_3Co_4O_9$. Compared to pure $Ca_3Co_4O_9$, the ZnO-doped samples exhibit a more significant reduction in their thermal conductivity. Specifically, the κ of pure $Ca_3Co_4O_9$ was 2.58 W m^{-1} K^{-1} at a temperature of 825 K, whereas that of the

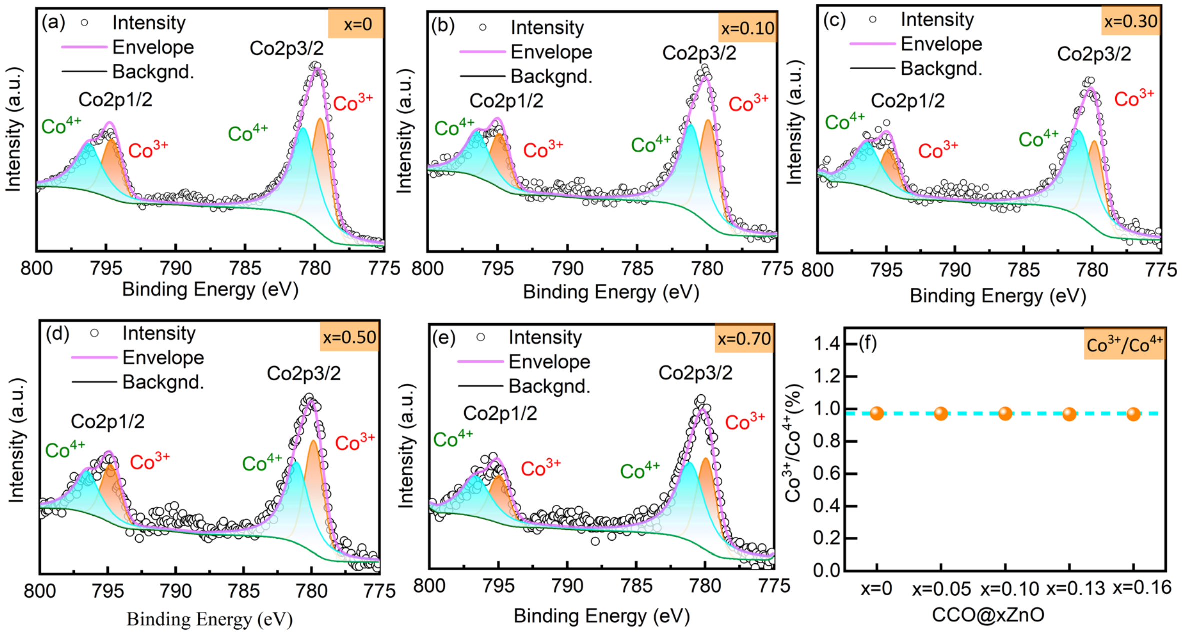

Fig. 3 (a–e) Co ion split peak fitting curves for CCO@*x*ZnO and (f) relative Co^{3+} and Co^{4+} contents in the samples.

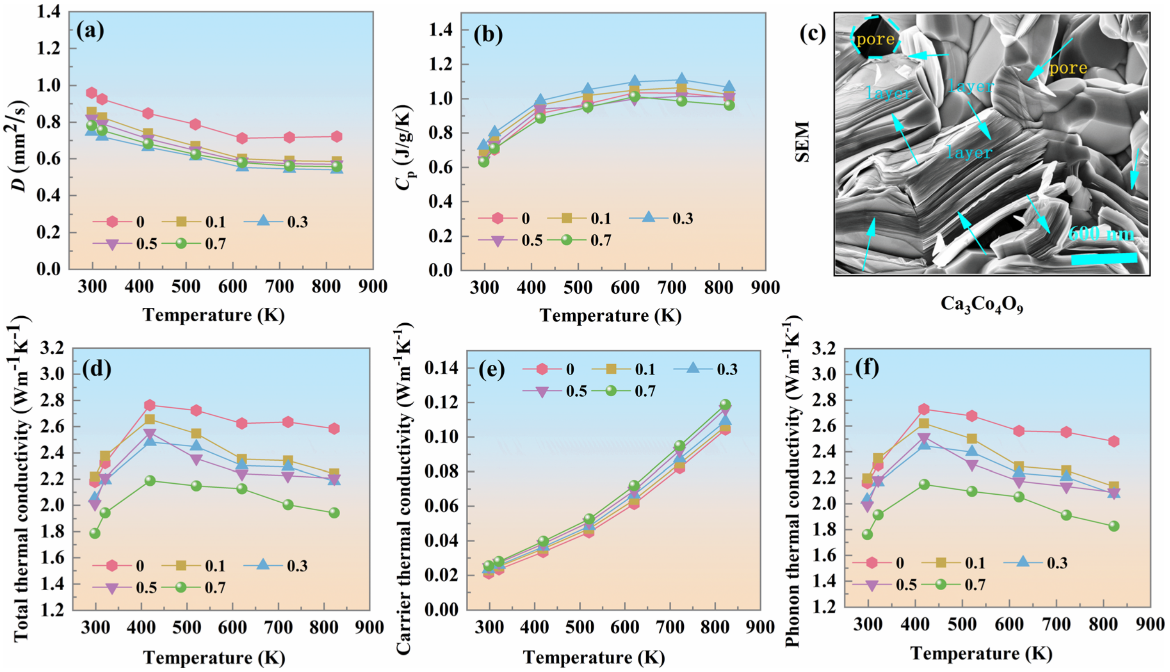

Fig. 4 (a) D; (b) C_p; (c) layered structure; (d) κ_{tot}; (e) κ_c; and (f) κ_l of CCO@xZnO.

CCO@0.7ZnO sample decreased to 1.94 W m^{-1} K^{-1}, a decrease of about 25%.

In the $Ca_3Co_4O_9$ system, the thermal conductivity is denoted as $\kappa = \kappa_c + \kappa_l$. According to the Wiedemann–Franz law, κ_c can be calculated through $\kappa_c = LT/\rho$ (L is the Lorentz constant). The calculation shows relatively tiny values of κ_c (Fig. 4e). Therefore, k is mainly affected by κ_l (Fig. 4f). According to Matthiessen's rule, κ_l is primarily governed by point defect scattering, grain boundary scattering, and non-simple harmonic three-phonon Umklapp scattering. Borrowing from the Debye model for analyzing the heat conduction of gas molecules, the phonon contribution to the heat conduction can be expressed as $\kappa_l = C_V vl$, where C_V, v, and l represent the constant volume heat capacity per unit volume, the phonon propagation velocity, and the mean free-range, respectively. C_V is an intrinsic property of the material.

ZnO doping reduces κ_l through multiple synergistic mechanisms. While increased density with higher ZnO content (Table 1) indicates reduced macro-porosity, which could potentially weaken pore-induced phonon scattering, the dominant effect arises from multi-scale interface engineering and defect-induced scattering. Specifically, nano-ZnO inclusions introduce dense heterogeneous interfaces between CCO and ZnO, with increasing ZnO content enhancing interface density and strengthening phonon barrier effects. Density mismatch between ZnO and the matrix induces localized crystal distortions, and the ionic radius difference between CCO and ZnO introduces stress field scattering, collectively intensifying mass fluctuation scattering. ZnO incorporation also reduces particle size, enhancing point defect scattering, while increased contact interfaces strengthen grain boundary scattering. Additionally, residual pores redistribute into nanoscale interfacial voids that scatter mid-frequency phonons more effectively than larger, isolated pores in undoped samples. These combined effects reduce phonon mean free path and propagation velocity, leading to significant κ_l suppression. Thus, ZnO doping effectively lowers the thermal conductivity of $Ca_3Co_4O_9$, consistent with the observed 25% reduction in κ for the CCO@0.7ZnO sample at 825 K.

The out-of-plane thermal conductivity (c-axis direction) was measured using laser flash method. The study revealed that compared to in-plane thermal conductivity, the out-of-plane thermal conductivity is relatively lower,[24,25] primarily attributed to enhanced phonon scattering effects at the interface between the layered structure and zinc oxide matrix. The c-axis direction inherently exhibits weak interlayer coupling characteristics, combined with the dispersed distribution of zinc oxide nanoparticles at grain boundaries, which collectively form additional barriers hindering phonon propagation. Consequently, the experimental results obtained in this study are lower than those measured in-plane.

Theoretical modelling of thermal conductivity of composites. Many factors influence the thermal conductivity properties of composites, primarily the thermal conductivity of both the additive and the matrix material, the spatial arrangement of the additive particles, the thermal resistance at the interfaces between materials, and the pore structure introduced during the preparation of the composites (Fig. 5a). Notably, the thermal conductivity of ZnO is relatively high at room temperature, about 25 W m^{-1} K^{-1}, a value that significantly exceeds that of $Ca_3Co_4O_9$. However, the experimental results showed that the thermal conductivity of the composites showed a decreasing trend with increasing ZnO content. The internal particle phase distribution of the composites obtained by thorough blending

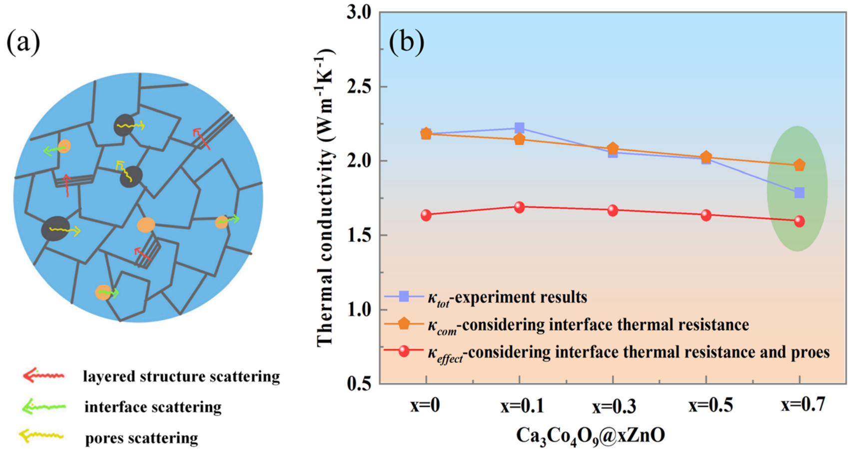

Fig. 5 (a) Schematic diagram of factors affecting thermal conductivity. (b) CCO@*x*ZnO considering interfacial thermal resistance, considering interfacial thermal resistance and porosity, and actual measured thermal conductivity value.

and compression molding of ZnO and $Ca_3Co_4O_9$ was considered uniform. Therefore, particle distribution had minimal impact on the composites' thermal conductivity under these experimental conditions. However, interfaces in the composites will undoubtedly significantly impact the thermal conductivity properties. To describe this phenomenon more accurately. Pang based on the effective medium heat transfer theory to optimize the traditional series-parallel model and then gave a composite unit effective thermal conductivity model considering the interface thermal resistance effect, denoted by κ_{com}[26]

$$k_{\text{com}} = k_2 + \frac{\pi B^{-1}}{A} - \pi k_2 B^{-2} + \frac{\pi\left(\frac{B}{k_2} + \frac{2R_{\text{B}}}{R}\right)\ln\left(\frac{\frac{B}{k_2} + \frac{2R_{\text{B}}}{R}}{2A + \frac{B}{k_2} + \frac{2R_{\text{B}}}{R}}\right)}{2BA^2} \tag{1}$$

where A, B and V_1 are respectively:

$$A = \frac{1}{k_1} - \frac{1}{k_2}$$
$$B = \sqrt[3]{\frac{4\pi}{3V_1}} \tag{2}$$
$$V_1 = \frac{\rho_{\text{comp}} - \rho_{\text{CCO}}}{\rho_{\text{theo,ZnO}} - \rho_{\text{CCO}}} \times \frac{w_{\text{ZnO}}}{\rho_{\text{theo,ZnO}}}$$

The κ_2 represents the thermal conductivity of $Ca_3Co_4O_9$, while κ_1 corresponds to the thermal conductivity of ZnO. V_1 refers to the composite material's volume fraction of the ZnO, where ρ_{comp} is the measured composite density, $\rho_{\text{CCO}} = 3.559\ \text{g cm}^{-3}$ and $\rho_{\text{theo,ZnO}} = 5.610\ \text{g cm}^{-3}$ are theoretical densities, and ZnO is the weight fraction. The results calculated based on the above formulas are as follows: 0, 0.001, 0.006, 0.011, 0.016. R_{B} indicates the interfacial thermal resistance between the ZnO particles and the $Ca_3Co_4O_9$ matrix, which is about $4.0 \times 10^{-9}\ \text{m}^2\ \text{K}^{-1}\ \text{W}^{-1}$.[27] R denotes the diameter of ZnO. It is significant to mention that the particle size of $Ca_3Co_4O_9$ in this research is about 700 nm, whereas the ZnO particles are much smaller, with a size of about 50 nm. Consequently, within the analytical framework of this study, ZnO particles can be approximated as small spherical entities. The specific values for the relevant parameters are provided in Table 2 for use in further analyses and calculations. Upon accounting for the interfacial thermal resistance, the thermal conductivity of $Ca_3Co_4O_9$ with ZnO content introduced at ambient temperature can be evaluated—the effective thermal conductivity κ_{com}, calculated as given in Fig. 5b.

When examining ceramic-like substances, it is essential to account for how porosity influences thermal conductivity. Pang *et al.*[26] extended the modeling approach outlined in eqn (2) to understand better how pores contribute to thermal conductivity. The model depicted the composite material as a single-phase solid characterized by effective thermal conductivity, κ_{com}, while considering the pores as a separate phase. Pang *et al.* employed this method to create a detailed thermal conductivity model for composites, factoring in the influence of voids and interface thermal impedances.

In this model, the researchers calculated the composite material's effective thermal conductivity (κ_{effect}), capturing the combined impact of factors such as porosity, interfacial thermal resistance, and the material's inherent properties on its overall thermal performance. This approach provides a holistic understanding of how these elements influence thermal conductivity. This research result is of great significance for the deep understanding of the heat conduction mechanism of ceramic-like materials, as well as guiding the development and optimization of related materials. The related derivation process and the final obtained expression of κ_{effect}:[26]

$$\frac{1}{k_{\text{effect}}} = \frac{1 - 1.24\xi^{\frac{1}{3}}}{k_{\text{com}}} + \frac{1}{0.65(k_{\text{air}} - k_{\text{com}})\xi^{\frac{1}{3}} + 0.81k_{\text{com}}\xi^{-\frac{1}{3}}} \tag{3}$$

The thermal conductivity of the porous phase is κ_{air}, and the porosity ξ represents the proportion of pores in the composite

Table 2 Corresponding values of parameters used in κ_{com} and κ_{effect} calculations

Symbol	Meaning	Value
κ_1	Thermal conductivity of matrix material	25 W m^{-1} K^{-1}
κ_2	Thermal conductivity of the additive	2.2 W m^{-1} K^{-1}
V_1	Volume fraction of the additive phase	0; 1.7%; 5.4%; 8.9%; 12.5%
R	Additive phase diameter of the particles	50 nm
R_{B}	Interfacial thermal resistance of ZnO	4.0×10^{-9} m^2 K W^{-1}
κ_{air}	Air thermal conductivity	0.023 W m^{-1} K^{-1}

unit cell. This parameter can be calculated by the formula $\xi = (\rho_0 - \rho_i)/\rho_0$, where ρ_0 is the theoretical density value of the matrix material $Ca_3Co_4O_9$, which was set to 4.68 g cm^{-3}, and ρ_i represents the measured density of the individual measured density of a specific sample. Its values are detailed in Table 1. We analyze how pores and interfacial thermal resistance influence the thermal conductivity of CCO@ZnO, treating interfacial effects as a unified phase according to eqn (2). In contrast, the pores are regarded as another independent phase. In this context, κ_{air} is set to be the thermal conductivity of the air in the stomata (0.023 W m^{-1} K^{-1}). Using these parameters and eqn (3), we calculated the composite's effective thermal conductivity, κ_{effect}, containing stomata and interfacial thermal resistance. Results of the calculations are shown in Fig. 5b for visual analysis.

From the data in Fig. 5b, considering only the interfacial thermal resistance factor, the κ_{com} of CCO@*x*ZnO shows a decreasing trend as the ZnO addition is increased, and this trend coincides with the experimentally measured κ values. This indicates that adding ZnO introduces more interfaces, which serve as barriers to heat transfer, thereby lowering the thermal conductivity. Moreover, it is essential to recognize how stomata influence the κ_{effect} in our analysis. It is found that the value of κ_{effect} also shows a decreasing trend with the increase of ZnO addition, and this decrease is more significant compared to κ_{com}. Especially at high temperatures, the κ_{effect} value is closer to the experimentally measured k value. This phenomenon strongly indicates that pores significantly affect the effective thermal conductivity of the composite material.

To sum up, by incorporating ZnO into $Ca_3Co_4O_9$, we successfully introduced two mechanisms to reduce thermal conductivity: interfacial thermal resistance and porosity. This result highlights ZnO as a viable approach to reducing thermal conductivity in $Ca_3Co_4O_9$ while offering a solid theoretical foundation and practical insights for further optimizing the thermal conductivity characteristics in such composites.

Electrical conductivity

Fig. 6a depicts the electrical conductivity trend with temperature for a series of samples of CCO@*x*ZnO, exhibiting typical semiconductor conducting properties of these samples, *i.e.*, the electrical conductivity gradually increases with increasing temperature. The electrical conductivity of the samples shows a slight enhancement trend as the ZnO ratio increases. In particular, when the ZnO addition reaches 0.7, its electrical conductivity reaches 62.45 S cm^{-1} at 1080 K, about 11% higher than the undoped pure $Ca_3Co_4O_9$ sample at the same temperature.

We interpreted the experimental results using a small polariton hopping conduction model, under which the electrical conductivity of CCO@*x*ZnO can be expressed as a function of the constants A, which is tied to the scattering mechanism, the carrier concentration n, the carrier power e, jumps distance a, the Boltzmann constant k_{B} depending on the scattering mechanism $\sigma(T) = (Anea^2/T)e^{-\frac{E_a}{k_{\mathrm{B}}T}}$. This equation emphasizes that the activation energy is an essential factor in determining the electrical conductivity and the carrier concentration. To quantify the activation energy, we further analyzed the plot of $\ln(\sigma T)$ *versus* $1000/T$ presented in Fig. 6b and derived the activation energies within different temperature intervals (Region A: 850–450 K; Region B: 450–300 K) by linear fitting (the goodness-of-fit R^2 was as high as 0.99).

To quantify the activation energy, we further analyzed the plot of $\ln(\sigma T)$ *versus* $1000/T$ presented in Fig. 6b and derived the activation energies within different temperature intervals (Region A: 850–450 K; Region B: 450–300 K) by linear fitting (the goodness-of-fit R^2 was as high as 0.99). Fig. 6c illustrates the fitting results, showing that the activation energy is stable at about 0.3 eV within Region B. In contrast, in Region A, the activation energy fluctuates with increased ZnO doping. The fluctuation of activation energy in the higher temperature region with increasing ZnO content arises from the competitive interplay of three key mechanisms. First, nonlinear interfacial charge transfer: low ZnO content lowers activation energy *via* sufficient charge transfer; moderate content raises it due to agglomeration-induced hole over-compensation; high content reverses the trend as agglomeration reduces interfacial efficiency. Second, dynamic defect evolution: ZnO-induced oxygen vacancies and fluctuating Co^{3+}/Co^{4+} valence states (with differing ionization energies) disrupt stability. Third, temperature-dependent stress scattering: uniform stress at low content eases with heat, lowering activation energy; moderate-to-high content causes stress concentration (raising it) and excessive agglomeration triggers "stress shielding" (slightly lowering it). These coupled effects reflect the transition from lattice-dominated to interface-scattering-dominated transport, driving the fluctuation. These coupled effects reflect the transition from intrinsic lattice-dominated to interface-scattering-dominated carrier transport, resulting in the observed activation energy fluctuations.

Furthermore, the size difference between the nano-ZnO ($\approx$50 nm) and $Ca_3Co_4O_9$ matrix particles ($\approx$700 nm) is

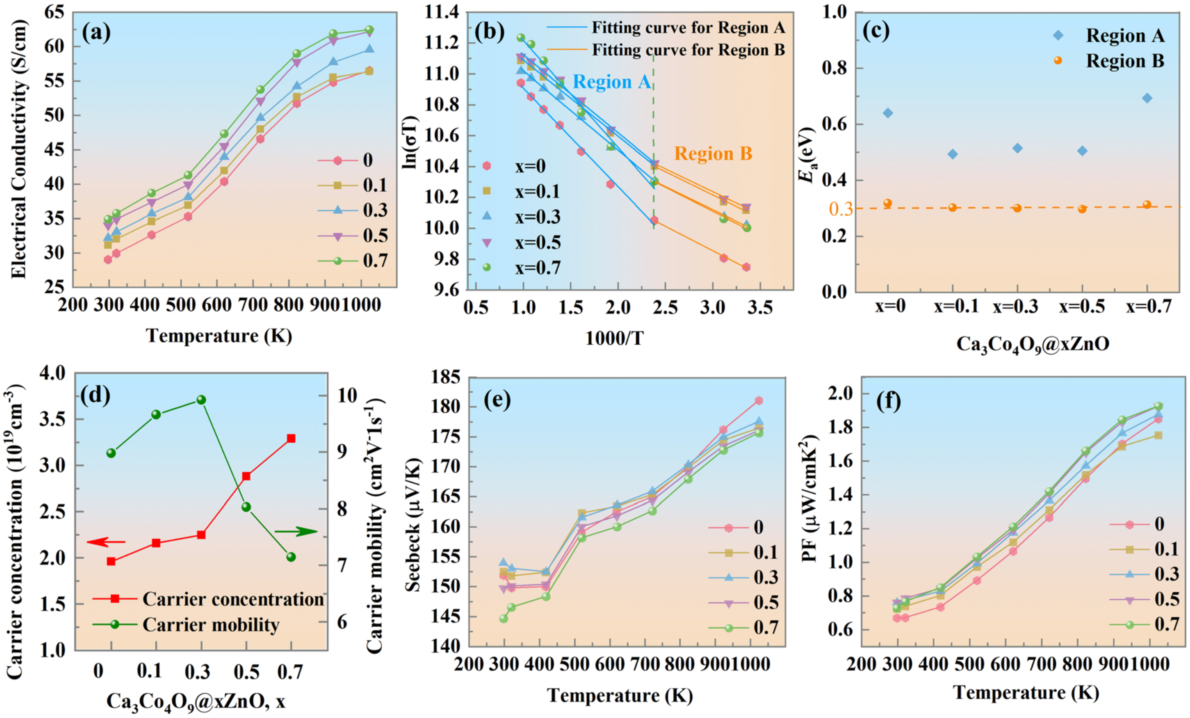

Fig. 6 Plots of (a) conductivity *versus* temperature, (b) ln(*T*) *versus* 1000/*T*, (c) E_a, (d) carrier concentration and mobility (e) Seebeck coefficient *versus* temperature, and (f) PF *versus* temperature for CCO@*x*ZnO.

pivotal in regulating the electrical transport properties of the composites: nano-ZnO tends to distribute in the pores of the CCO matrix, optimizing electron transport paths and enhancing heterojunction interfacial interactions. Hall test results (Table 3) confirm hole-dominated conduction (positive Hall coefficients) and reveal a continuous increase in carrier concentration with rising ZnO content, which is primarily attributed to charge transfer at the ZnO-CCO heterojunction interface and defect regulation—an effect unaffected by the mobility variation trend. The carrier mobility exhibits a "first increase then decrease" trend, driven by evolving scattering mechanisms: at low ZnO content, uniform dispersion of nanoparticles optimizes the interface structure, reducing intrinsic defect scattering centers in CCO and suppressing random carrier scattering at grain boundaries, thereby increasing mobility; at excessive ZnO content, a sharp rise in grain boundary density, coupled with local agglomeration and potential lattice distortion, intensifies carrier scattering between multiple grain boundaries, leading to decreased mobility. The overall increasing trend in electrical conductivity with ZnO content arises from the synergistic effect of carrier concentration and mobility ($\sigma = en\mu$), where the dominant positive contribution of continuously increasing carrier concentration outweighs the negative impact of later-decreasing mobility, resulting in enhanced conductivity.

Moreover, the electrical conductivity measured by the four-probe method primarily reflects the in-plane (*ab*-plane) transport behavior. The in-plane electrical conductivity ($\sigma_{\parallel}$) exhibits higher values due to the intrinsic layered structure of the $Ca_3Co_4O_9$ matrix and the strong texture induced by uniaxial pressing along the *ab*-plane. In this direction, carrier transport benefits from reduced lattice scattering and continuous intra-layer conduction paths. The introduction of ZnO nanoparticles further optimizes in-plane electrical conductivity by enhancing interfacial charge transfer and reducing defect scattering within the *ab*-plane, contributing to the observed increasing trend with ZnO content.

Table 3 Electrical conductivity σ, resistivity ρ, carrier concentration n, carrier mobility μ, Hall coefficient R_H and f factor of CCO@*x*ZnO samples at 300 K

Sample	σ (S cm^{-1})	ρ (Ω cm^{-1})	n (10^{19} cm^{-3})	μ (cm^2 V^{-1} S^{-1})	R_H (cm^{-3} C^{-1})	f
CCO	28.186	0.035	1.962	8.979	0.319	0.975
CCO@0.1ZnO	33.378	0.030	2.159	9.663	0.289	0.998
CCO@0.3ZnO	35.677	0.028	2.247	9.923	0.278	0.997
CCO@0.5ZnO	37.021	0.027	2.887	8.031	0.217	0.998
CCO@0.7ZnO	37.604	0.027	3.288	7.148	0.190	0.981

Seebeck coefficient

The variation of the Seebeck coefficient with temperature for the CCO@*x*ZnO series of samples is given in Fig. 6e. The *S* of the samples rises when the temperature varies from 400 K to 1080 K. All the samples have positive Seebeck coefficient values and exhibits p-type semiconductors. This is consistent with the results in Table 3 where the Hall coefficient is positive, that is, holes are still the main carrier. In the pristine $Ca_3Co_4O_9$ sample, the hole conduction mechanism mainly originates from the mixed valence states of Co elements. The introduction of ZnO affects carrier transport properties primarily through interface effects and defect regulation. XRD and XPS results demonstrate that Zn does not substitute at Ca or Co sites, indicating the absence of chemical doping.

The *S* of ZnO-added samples have a slight decrease compared to pure $Ca_3Co_4O_9$. It can be analyzed from two aspects. The *S* of the semiconductor material with the composite of two substances can be expressed as:

$$S_{\mathrm{TOT}} = \sum_i \sigma_i S_i \bigg/ \sum_i \sigma_i \quad (4)$$

S_{TOT} denotes the total obtained Seebeck, σ_{i}, and S_{i} denotes the electrical conductivity and *S* of different substances. The electrical conductivity has a greater impact on the value *S*, as improved electrical conductivity increases the denominator. In contrast, the Seebeck coefficient of ZnO itself is smaller with less molecular variation. This results in a lower *S* for the composite samples.

On the other hand, from the analysis of micro mechanism, as shown in Table 3, when ZnO exists only as nanoscale inclusions, the carrier concentration *n* increases with the increase of ZnO content, which is attributed to the interfacial physical effects, among which the interfacial charge transfer is the main factor. According to the band bending effect, when ZnO (work function ≈5.2 eV) contacts with $Ca_3Co_4O_9$ (≈4.8 eV), a Type-II heterojunction is formed, leading to the redistribution of interfacial charges. Electrons flow from $Ca_3Co_4O_9$ to ZnO, resulting in the increase of hole concentration in the composite. Meanwhile, the change of carrier concentration has a direct impact on the *S* (consistent with the Pisarenko relation: $S \propto 1/n$). Consequently, the *S* decreases slightly with the increase of ZnO content, which is mainly caused by the increase of carrier concentration due to the additional holes introduced by interfacial defects.

In Fig. 6f, PF ($\mathrm{PF} = \sigma S^2$) curves with temperature are demonstrated for a series of samples of CCO@*x*ZnO. The graph shows a gradual increase in PF as the temperature rises. This phenomenon results from the combined effect of electrical conductivity and the Seebeck coefficient, indicating that the addition of ZnO can effectively regulate the power factor of the sample. The PF value of the CCO@0.7ZnO improved to 1.93 μW cm^{-1} K^{-2} at 1080 K, up from 1.85 μW cm^{-1} K^{-2} for the undoped pure $Ca_3Co_4O_9$. This finding provides a new perspective for optimizing the thermoelectric characteristics of $Ca_3Co_4O_9$ through ZnO doping.

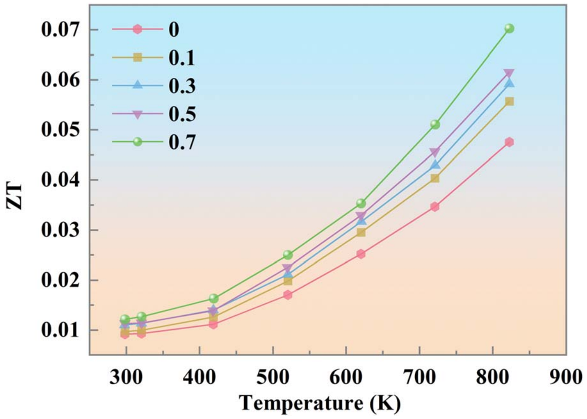

Fig. 7 *ZT* values with temperature for CCO@*x*ZnO.

Thermoelectric figure of merit

Fig. 7 illustrates the temperature-dependent *ZT* trend for the CCO@*x*ZnO series, determined by the formula $ZT = \sigma S^2 T/(\kappa_{\mathrm{c}} + \kappa_{\mathrm{l}})$. All samples show an increasing *ZT* with rising temperature, resulting from the interplay of electrical conductivity, the Seebeck coefficient, and thermal conductivity. Notably, the *ZT* of the CCO@0.7ZnO sample hits 0.07 at 825 K, which is an improvement of about 75% compared with the undoped pure $Ca_3Co_4O_9$ sample (0.04). This result powerfully demonstrates that adding a moderate amount of ZnO can significantly improve the thermoelectric properties of $Ca_3Co_4O_9$, which provides a strategy for fine-tuning the characteristics of thermoelectric materials.

Conclusions

This study methodically examines the thermoelectric conductivity characteristics of CCO@*x*ZnO synthesized *via* the sol–gel technique. The thermal conductivity of pure $Ca_3Co_4O_9$ is 2.58 W m^{-1} K^{-1} at 825 K, while that of the $Ca_3Co_4O_9$@0.7ZnO sample decreases to 1.94 W m^{-1} K^{-1}, which is a decrease of about 25%. The effective medium theory indicates that adding ZnO to $Ca_3Co_4O_9$ enhances porosity and introduces interfacial thermal resistance, both reducing thermal conductivity. This finding underscores the significant role ZnO plays in diminishing the thermal conductivity of $Ca_3Co_4O_9$, effectively confirming its impact. In addition, adding ZnO enhances the electrical conductivity of $Ca_3Co_4O_9$. At 1080 K, the sample with $x = 0.7$ exhibits an electrical conductivity of 62.45 S cm^{-1}, marking an 11% rise compared to the pure sample under identical conditions. However, Notably, the *S* of the ZnO-added slightly decreases compared to the pure $Ca_3Co_4O_9$. Nevertheless, the PF of the CCO@0.7ZnO sample at 1080 K still reached 1.93 μW cm^{-1} K^{-2}, which is an improvement compared to the pure $Ca_3Co_4O_9$ sample (1.85 μW cm^{-1} K^{-2}). With the synergistic effect of thermal and electrical properties, the *ZT* of the CCO@0.7ZnO sample reached 0.07 at 825 K, which is an improvement of about 75% as compared to the *ZT* of the pure

$Ca_3Co_4O_9$ sample (0.04). This improvement indicates that the ZnO doping effectively enhances the thermoelectric properties of $Ca_3Co_4O_9$.

Author contributions

Yanan Li: Synthesis, characterization, data curation, writing – original draft. Ping Wu: conceptualization, project administration. Shuai Ma: supervision, writing – review & editing. Mingdi Zhang: visualization. Yili Pei: resources.

Conflicts of interest

There are no conflicts to declare.

Data availability

The authors declare that the data supporting the findings of this study are available within the paper. Should any raw data files be needed in another format they are available from the corresponding author upon reasonable request. See DOI: **https://doi.org/10.1039/d5ra04876a**.

Acknowledgements

This work is sponsored by the Youth Research Special Project of NCUT (No. 2025NCUTYRSP058); North China University of Technology Physics Innovation Laboratory Construction Project (108051360024XN232); Tianjin Natural Science Foundation (No. 24JCQNJC00380); China Postdoctoral Science Foundation (2023M734282); Tianjin Education Commission Research Program Project (2023KJ206); Research start-up fund of NCUT (11005136025XN076-086).

References

1 S. Liu, S. Bai, Y. Wen, J. Lou, Y. Jiang, Y. Zhu, D. Liu, Y. Li, H. Shi, S. Liu, L. Wang, J. Zheng, Z. Zhao, Y. Qin, Z. Liu, X. Gao, B. Qin, C. Chang, C. Chang and L.-D. Zhao, *Science*, 2025, **387**, 202–208.
2 K. Toko, S. Maeda, T. Ishiyama, K. Nozawa, M. Murata and T. Suemasu, *Adv. Electron. Mater.*, 2024, 2400130.
3 Y. Gong, P. Ying, Q. Zhang, Y. Liu, X. Huang, W. Dou, Y. Zhang, D. Li, D. Zhang and T. Feng, *Energy Environ. Sci.*, 2024, **17**, 1612–1623.
4 Y. Yu, A. Sheskin, Z. Wang, A. Uzhansky, Y. Natanzon, M. Dawod, L. Abdellaoui, T. Schwarz, C. Scheu and M. Wuttig, *Adv. Energy Mater.*, 2024, **14**, 2304442.
5 T. Deng, Z. Gao, Z. Li, P. Qiu, Z. Li, X. Yuan, C. Ming, T.-R. Wei, L. Chen and X. Shi, *Science*, 2024, **386**, 1112–1117.
6 L. Su, D. Wang, S. Wang, B. Qin, Y. Wang, Y. Qin, Y. Jin, C. Chang and L.-D. Zhao, *Science*, 2022, **375**, 1385–1389.
7 S. Kalaimathi and K. S. Babu, *Surf. Interfaces*, 2024, **47**, 104208.
8 S. Bhoobash, N. Pradhan and C. Behera, *J. Mater. Sci.: Mater. Electron.*, 2023, **34**, 1964.
9 I. A. Leonidov and E. I. Konstantinova, *J. Alloys Compd.*, 2025, 1010.
10 Z. Lou, Z. Wei, J. Gou, J. Xu, C. Gong and F. Gao, *ACS Appl. Energy Mater.*, 2024, **7**, 12119–12130.
11 N. Kanas, B. A. D. Williamson, F. Steinbach, R. Hinterding, M.-A. Einarsrud, S. M. Selbach, A. Feldhoff and K. Wiik, *ACS Appl. Energy Mater.*, 2022, **5**, 12396–12407.
12 Z. Han, J. Zhang, H. Ma, F. Xing, Y. Qi, J. Wei, G. He, Y. Zhang, Y. Xin, Q. Wang and Z. Shi, *ACS Appl. Mater. Interfaces*, 2025, **17**, 5114–5123.
13 J. F. Fang, H. Yang, L. Liu, Q. Kang and Y. C. Gou, *J. Mater. Sci.*, 2024, **59**, 2228–2257.
14 Y. Shimizu, K. Hayashi and Y. Miyazaki, *Solid State Sci.*, 2024, **152**, 107536.
15 J. Martin, L. Wang, L. Chen and G. Nolas, *Phys. Rev. B: Condens. Matter Mater. Phys.*, 2009, **79**, 115311.
16 J. Zhou, X. Li, G. Chen and R. Yang, *Phys. Rev. B: Condens. Matter Mater. Phys.*, 2010, **82**, 115308.
17 W. W. Sun, W. H. Fan, S. P. Chen, Y. Y. Li and Q. S. Meng, *Adv. Nanosci. Nanotechnol.*, 2012, **465**, 292–295.
18 R. K. Gupta, R. Sharma, A. K. Mahapatro and R. P. Tandon, *Phys. B*, 2016, **483**, 48–53.
19 X. Wang, X. C. Liu, W. Yan, S. Hou and X. Liu, *J. Alloys Compd.*, 2019, **785**, 698–705.
20 F. Delorme, P. Diaz-Chao, E. Guilmeau and F. Giovannelli, *Ceram. Int.*, 2015, **41**, 10038–10043.
21 Y.-n. Li, P. Wu, S. Zhang, Y. Pei, J. Yang, S. Chen and L. Wang, *Ceram. Int.*, 2022, **48**, 33967–33975.
22 W. B. Guan, L. Y. Zhang, C. Wang and Y. X. Wang, *Mater. Sci. Semicond. Process.*, 2017, **66**, 247–252.
23 B. C. Luo, J. Wang, M. M. Duan, K. X. Jin and C. L. Chen, *Mater. Lett.*, 2014, **120**, 133–135.
24 C. H. Lim, W. S. Seo, S. Lee, Y. S. Lim, J. Y. Kim, H. H. Park, S. M. Choi, K. H. Lee and K. Park, *J. Korean Phys. Soc.*, 2015, **66**, 794–799.
25 D. Kenfaui, D. Chateigner, M. Gomina and J. G. Noudem, *Int. J. Appl. Ceram. Technol.*, 2011, **8**, 214–226.
26 X. M. Pang, J. Q. Zhou, J. X. Yang and M. H. Liao, *Chin. J. Nonferrous Met.*, 2015, **26**, 1668–1674.
27 X. Liang and L. Shen, *Acta Mater.*, 2018, **148**, 100–109.